Optics Letters

Ultra-low-threshold InGaN/GaN quantum dot micro-ring lasers

Danqing Wang,[1,*] Tongtong Zhu,[2] Rachel A. Oliver,[2] and Evelyn L. Hu[1,3]

[1]John A. Paulson School of Engineering and Applied Sciences, Harvard University, Cambridge, Massachusetts 02138, USA
[2]Department of Materials Science and Metallurgy, University of Cambridge, Cambridge CB3 0FS, UK
[3]e-mail: ehu@seas.harvard.edu
*Corresponding author: danqing@seas.harvard.edu

Received 11 December 2017; revised 14 January 2018; accepted 15 January 2018; posted 16 January 2018 (Doc. ID 315014); published 9 February 2018

In this work, we demonstrate ultra-low-threshold, optically pumped, room-temperature lasing in GaN microdisk and micro-ring cavities containing InGaN quantum dots and fragmented quantum wells, with the lowest measured threshold at a record low of 6.2 μJ/cm^2. When pump volume decreases, we observe a systematic decrease in the lasing threshold of micro-rings. The photon loss rate, γ, increases with increasing inner ring diameter, leading to a systematic decrease in the post-threshold slope efficiency, while the quality factor of the lasing mode remains largely unchanged. A careful analysis using finite-difference time-domain simulations attributes the increased γ to the loss of photons from lower-quality higher-order modes during amplified spontaneous emission.

OCIS codes: (140.0140) Lasers and laser optics; (140.3945) Microcavities; (140.3948) Microcavity devices.

https://doi.org/10.1364/OL.43.000799

Exploring the limits of low-threshold lasing has been one of the central goals in the development of nanocavity lasers. GaN-based microdisk cavities provide the advantages of high-quality factors (Qs) and small modal volumes, and have already demonstrated their applicability for low-threshold lasers [1–7]. We have previously observed lasing in 1 μm diameter microdisks containing three layers of InGaN quantum dots (QDs) with lasing thresholds as low as 0.28 mJ/cm^2 [4]. A distinct advantage of the microdisk lies in the high-Q factors of the whispering gallery modes (WGMs), with only a few modes that overlap with the gain region. The high-Q WGMs are confined to the periphery of the microdisks; therefore, the inner volume of the microdisk structure is a less efficient contributor to the lasing process, since it may act as an energy sink and absorb part of the pump power, in competition with the lasing process. Thus, micro-ring structures, where the inner volume of the microdisks is removed, should exhibit lower lasing thresholds. Accordingly, and for the purpose of comparison, we fabricated micro-ring laser structures with different geometries, using active layers comprising three layers of InGaN QDs, as well as microdisks of the same gain layer composition. We indeed observed a systematic decrease in the lasing threshold as we removed volume from the micro-rings, with the lowest lasing threshold measuring 6.2 μJ/cm^2.

As the threshold decreases with greater volume removal, the post-threshold slope efficiency also decreases. The implication is that we have decreased the lasing threshold even in the presence of photon loss. Fortunately, the discrete modes of the micro-rings and microdisks provide us with a sensitive picture of the dynamic changes in the laser structures, giving us an understanding of where the photon loss occurs in a way that is compatible with the lowered thresholds.

The material used in this work is grown by metal-organic vapor phase epitaxy (MOVPE) and consists of three $In_{0.2}Ga_{0.8}N$ QDs gain layer(s) in the middle of a 200 nm membrane of intrinsic GaN. The QDs are formed through a modified droplet epitaxy (MDE) method [8], and have an areal density of approximately 1×10^{10} cm^{-2}. Below the 200 nm cavity membrane is a 200 nm layer of $In_xGa_{1-x}N/In_yGa_{1-y}N$ sacrificial superlattice ($x = 5.1\%, y = 6.5\%$), which rests on top of an n-GaN pseudo substrate overlying the sapphire substrate. This structure has been described in previous work [4]. It should be noted that InGaN QDs formed through MDE are always associated with an accompanying network of interlinked InGaN strips—referred to as the fragmented quantum well (fQW) layer—approximately 2.5–3 nm in thickness. An atomic force micrograph of uncapped InGaN QD layer is shown in Fig. 1(a), and the cross-sectional composition of the gain layer is shown schematically in Fig. 1(b). This suggests that while in some areas QDs form upon the underlying GaN and will be entirely surrounded by GaN in the capped structure, in other areas QDs form on top of underlying InGaN fQW material. Further details of the growth of the full sample structure and the QDs can be found in [9,10].

The microdisks and micro-rings are fabricated by first depositing a 5 nm layer of SiO_2, followed by a thin metal

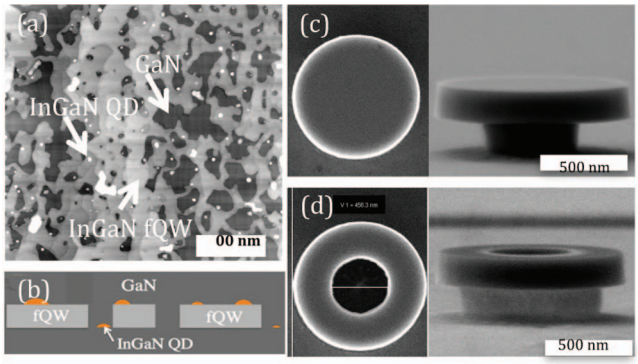

Fig. 1. (a) AFM images of uncapped InGaN epilayers on GaN. The bright spots are indium droplets that form InGaN QDs during growth of the GaN capping layer. The lighter gray area shows a network of interlinking InGaN strips, also known as fQWs, and the darker regions are bare GaN. (b) Schematic showing the active layer composition. (c) Top and side view SEM images of a microdisk and (d) a micro-ring of inner diameters $d_i = 500$ nm.

conductive layer to prevent charging during the subsequent e-beam lithography. Approximately 500 nm of FOX-16 negative electron-beam (e-beam) resist is then spun evenly onto the sample. We use e-beam lithography to pattern the FOX-16 into 1 μm diameter microdisks, as well as micro-rings with a 1 μm outer diameter and inner diameters of $d_i = 200$ nm, 400 nm, and 500 nm, respectively. These structures serve as the hard masks during inductively coupled plasma etching, which operates at 500 W in a nitrogen/chlorine environment with a flow rate of 25/25 sccm. Once the pattern has been transferred into the GaN material, we evaporate a Ti/Pt metal grid onto our sample which serves as the cathode during photoelectrochemical (PEC) etching, a bandgap-selective process that selectively etches the sacrificial superlattice into a post, creating an air gap and thus providing optical isolation between the suspended microstructure and the substrate beneath. Figures 1(c) and 1(d) show some representative SEM images of the completed microdisk and micro-rings.

The devices are optically pumped using a frequency doubled, pulsed, titanium-sapphire laser emitting at 380 nm with a 76 MHz repetition rate and 200 ps pulse duration through a high (0.90) numerical aperture objective. The measurements are taken at room temperature, and the emitted light is collected through the same objective into a spectrometer. Q values of lasing modes are calculated using $\lambda/\Delta\lambda$ where λ is the emission wavelength and $\Delta\lambda$ is the full width half maximum at λ. The typical Q values for these devices range between 2,000 and 3,000.

In Fig. 2, we plot the light-in-light-out (I-O) curves of selected microdisk and micro-rings from each geometry group. By performing linear fits on the lasing curves, we identify lasing threshold as the pump power at which the fitted line intersects the x-axis. In calculating the values of threshold power, we take into consideration the fraction of excitation beam that is intercepted by the devices, the reflection at air-GaN interfaces, the material absorption coefficient, as well as the thickness of the gain layers, similar to the calculation methods used in [11]. There are two clear correlations in laser performance with the geometry of the micro-cavity: (a) a decrease in lasing

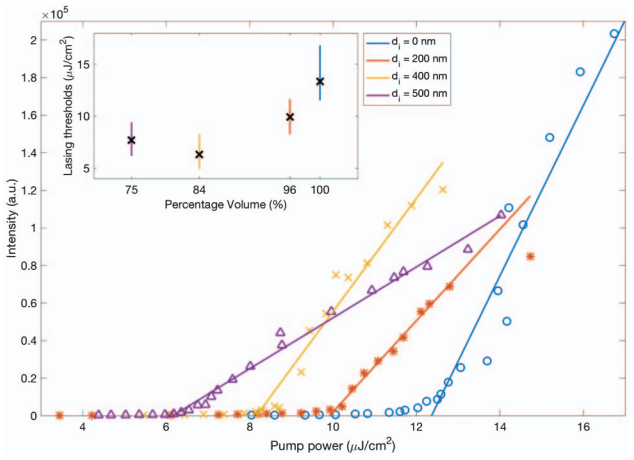

Fig. 2. Spread of lasing thresholds in microdisks and micro-rings of different geometries. The mean threshold in each geometry group, averaged over eight data points, is marked off with a cross. Inset: I-O curves of selected microdisk and micro-rings with 1 μm outer diameter, and different inner diameters of $d_i = 200$ nm, 400 nm, and 500 nm. As more volume is removed, the lasing threshold decreases from 93 μJ/cm^2 in the microdisk ($d_i = 0$ nm) to 79 μJ/cm^2 in a micro-ring with $d_i = 200$ nm, 70 μJ/cm^2 in a micro-ring with $d_i = 400$ nm, and 56 μJ/cm^2 in a micro-ring with $d_i = 500$ nm. The slope efficiency also decreases as more volume is removed.

threshold as the central volume is removed and (b) a concomitant decrease in post-threshold slope efficiency.

As observed from the four devices in Fig. 2, when more of the central volume is removed the lasing threshold decreases from 12 μJ/cm^2 in the microdisk ($d_i = 0$ nm) to 9.9 μJ/cm^2 in a micro-ring with $d_i = 200$ nm, 8.2 μJ/cm^2 in a micro-ring with $d_i = 400$ nm, and 6.2 μJ/cm^2 in a micro-ring with $d_i = 500$ nm. The inset to Fig. 2 shows the consistency in decreased threshold with the removal of the central volume for a set of eight devices. The mean threshold of each micro-ring-geometry, averaged over eight data points, is marked off on the plot with a cross. Thus, the removal of the center region, where the active layer material does not spatially overlap with the WGMs, indeed results in a lowering of the lasing thresholds.

Representative power-dependent emission spectra of a microdisk and a micro-ring ($d_i = 500$ nm), as shown in Figs. 3(a) (microdisk) and 3(b) (micro-ring), can provide us with additional insights into the lasing mechanisms. For both structures, the spectra at low pump power reveal two dominant high-Q

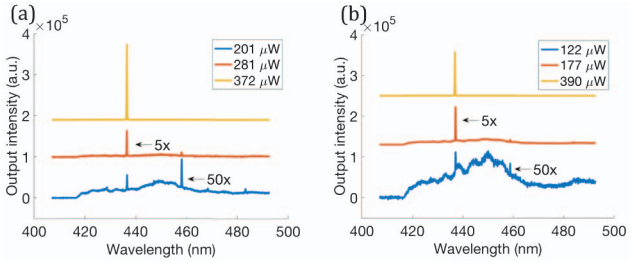

Fig. 3. Room-temperature lasing spectra of (a) a microdisk and (b) a micro-ring with $d_i = 500$ nm at increasing pump powers.

WGMs that overlap with the emission region of our heterogeneous InGaN gain material. The shorter wavelength mode of ~440 nm is attributed to emission from QDs and the longer wavelength mode of ~460 nm is attributed to emission from the fQWs [1,12,13]. In both the microdisk and the micro-ring, the highest intensity mode at low pump power is at the longer wavelength, although lasing ultimately occurs at the shorter, QD wavelength.

As discussed in previous work, the blue shift in wavelength with increased power is consistent with differing carrier capture efficiencies and hence photon emission of the QDs and fQWs in our material. At low pump powers, there is a much higher probability of carrier capture into the fQWs because of the larger areal coverage of the fQWs. The percentage of fQW is estimated at around 64 ± 3% based on four 2 μm × 2 μm AFM images of uncapped QD samples. As the pump power increases, the carrier capture probability into the QDs also increases. The QDs offer superior carrier confinement compared to the fQWs, favoring radiative recombination. In addition, they have a characteristic spontaneous lifetime between 1 and 5 ns, about 10 times shorter than that of the fQWs. The cavity mode, resonant with the QD emission wavelength, further augments the spontaneous emission rate of QDs in good spatial overlap with the WGMs, ultimately producing lasing at the shorter wavelengths characteristic of the QDs. A comparison of Figs. 3(a) and 3(b) highlights the differences in PL spectra at low pump power. The intensity of both WGMs is dramatically reduced in the micro-ring structure, with a greater reduction in the intensity of the longer wavelength (fQW) modes. The reduced "competition" of the longer wavelength mode also contributes to the QD lasing in the micro-ring structures.

How then do we account for the lowered post-threshold slope efficiency for the micro-ring structures, as shown in Fig. 2? Fits of our data to the coupled laser rate equations [14] reveal that the post-threshold slope efficiency shows greatest sensitivity to variations in the value of γ, the decay rate of photons from the cavity. Higher values of γ result in lower slope efficiencies. If, indeed, there is an increase in γ, or loss of photons associated with the micro-ring geometry, we expect to observe some degradation of the Q of the modes of the device, whereas the mode widths shown in Fig. 3 (related to Q values) show no degradation. In addition, one would imagine that greater photon loss would result in increased lasing thresholds.

We believe that the resolution to these issues relates to the role of the higher-order modes of the micro-ring structures, illustrated in the finite-difference time-domain (FDTD) simulations shown in Fig. 4. The field profiles of first-order (WGM) and higher-order modes and the corresponding spectra are modeled for two micro-rings with $d_i = 200$ nm and $d_i = 500$ nm, respectively. While the WGMs in both micro-ring structures have simulated Q values on the order of 100,000, the higher-order modes at $\lambda > 410$ nm are broadened (reduced Q, greater photon loss). For the disk with $d_i = 500$ nm, there is substantial overlap of the evanescent field of the higher-order mode with the inner boundary of the disk (indicated schematically by the solid red line), providing an easy visualization of the loss mechanism. Photons are lost from the higher-order modes at wavelengths that do not overlap with the QD emission wavelength responsible for lasing. This also explains why the changing micro-ring geometry does not affect the Q of the WGMs.

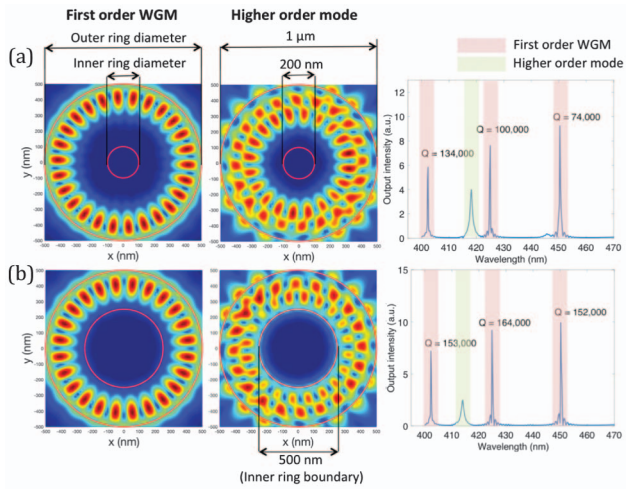

Fig. 4. FDTD simulation showing the field profile of the first- and higher-order modes of a micro-ring with (a) $d_i = 200$ nm and (b) $d_i = 500$ nm, as well as the cavity resonance wavelengths and simulated Q values for different modes. Red circles representing the inner and outer boundaries of the micro-rings are marked off on the diagrams.

To determine values of γ that correspond to our devices, we fit our lasing data to the characteristic "S-shape" curves of input versus output to more clearly delineate regions of sub-threshold operation, amplified spontaneous emission (ASE), and lasing. γ was used as the fitting parameter. The value of spontaneous emission lifetime of QDs used in our calculation is 1.9 ns, within the range of QD lifetimes from our experimental measurements, and the transparency carrier concentration is between 1.0×10^{26} m^{-3} and 1.1×10^{26} m^{-3}. Figure 5 shows an example of such a fit on a microdisk with a R^2 value of 0.97. All our fits have R^2 values ranging between 0.95 and 0.97, showing an excellent fit to the empirical data. The results are shown in Table 1, which indeed shows an increase in cavity decay rate, γ, with increased removal of the center volume. Table 1 also shows a correlation of cavity geometry with details of the fitted ASE region. As more material is removed from the center, the total contribution of ASE is reduced, likely reflecting the loss of "incoherent photons" from the cavity. ASE arises from the amplification of spontaneously emitted photons, which copy themselves by triggering stimulated emission events. The ASE region amplifies the intensity of photons of all phases, leading to the overall photon density in the cavity

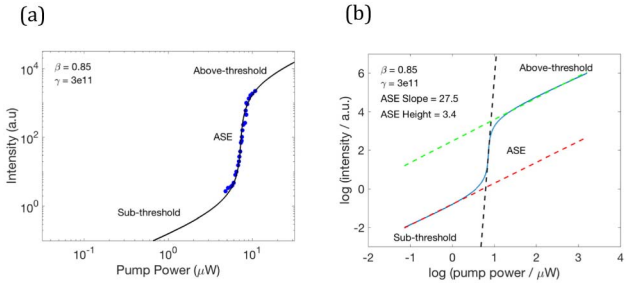

Fig. 5. (a) Fitted microdisk log-log lasing curves with $\beta = 0.85$ and $\gamma = 3 \times 10^{11}$, and (b) the fitted slope and height of the ASE region.

Table 1. Table of Fitted Values of the Cavity Decay Rate γ and ASE Height in Microdisk and Micro-Rings of Various Geometries

	Microdisk	400 nm Ring	200 nm Ring	500 nm Ring
Percentage Volume	100	84	96	75
Fitted γ (10^{12} s^{-1})	0.30	0.70	1.20	1.60
ASE Height	3.44	3.15	3.01	2.89

being incoherent, although there may exist local groups of coherent photons. Excess ASE is an unwanted effect in lasers as it can limit the maximum gain that can be achieved in the gain medium. The rather distinctive effects we observe relative to lowered lasing threshold accompanied by lowered slope efficiency and reduced ASE contribution may relate to the heterogeneous nature of our gain material, with two main contributors (QD and fQW) that influence different regions of the spectrum. Thus, we believe that photon emission from the fQWs dominates the ASE, and those photons overlap the lossier higher-order modes in the micro-ring structures. The selective loss of fQW photons, together with the reduced competition from fQW emission into a mode, produce the dramatically reduced threshold for lasing that we observe.

In conclusion, we have fabricated microdisk and micro-ring cavities containing three InGaN QD layers as the gain medium. The micro-ring lasers with increasing inner diameters show systematically lower values of lasing threshold. This threshold decrease is a result of the reduction in pump volume, as much of the fQW material is removed. Although the micro-ring geometry does not compromise the Q of the WGMs, there is a reduction of Q for higher-order modes for micro-rings with larger inner diameters. This results in increased photon loss, γ, producing a systematic decrease in the post-threshold slope efficiency with increased material removal from the center of the disk. Using γ as the fitting parameter, we observe an increased value of γ with increased micro-ring inner diameter. Our simulations indicate that the photons that are lost from the cavity are not correlated with emission from the QDs that ultimately produce lasing in our devices. Thus, our devices show both lowered lasing thresholds and lowered slope efficiencies with reduced central volume material.

The heterogeneous nature of our gain material, a combination of QDs and fQWs, together with the varying cavity geometries, gives us a detailed picture of the interactions between cavity modes and the microstructure of the gain material. Thus, the micro-ring geometry has given us substantial insight into the true limitations to low-threshold lasing, and how the input pump energy is allocated. These observations are important when considering which optimal nitride gain medium and cavity geometry to use to achieve lower-lasing threshold device design.

Funding. Engineering and Physical Sciences Research Council (EPSRC) (EP/H047816/1, EP/M011682/1); National Science Foundation (NSF) (1541959); Royal Academy of Engineering; Center for Nanoscale Systems (CNS).

Acknowledgment. This work was performed in part at the Center for Nanoscale Systems (CNS), a member of the National Nanotechnology Coordinated Infrastructure Network (NNCI), which is supported by the National Science Foundation. CNS is part of Harvard University. R. A. Oliver is grateful for support from a Royal Academy of Engineering/Leverhulme Trust Senior Research Fellowship.

REFERENCES

1. D. Simeonov, E. Feltin, H. J. Bühlmann, T. Zhu, A. Castiglia, M. Mosca, M. J. F. Carlin, R. Butté, and N. Grandjean, Appl. Phys. Lett. **90**, 061106 (2007).
2. D. Simeonov, E. Feltin, A. Altoukhov, A. Castiglia, J. F. Carlin, R. Butté, and N. Grandjean, Appl. Phys. Sci. **92**, 171102 (2008).
3. A. Woolf, T. Puchtler, I. Aharonovich, T. Zhu, N. Niu, D. Wang, R. A. Oliver, and E. L. Hu, Proc. Natl. Acad. Sci. USA **111**, 14042 (2014).
4. I. Aharonovich, A. Woolf, K. J. Russell, T. Zhu, N. Niu, M. J. Kappers, R. A. Oliver, and E. L. Hu, Appl. Phys. Lett. **103**, 021112 (2013).
5. A. C. Tamboli, E. D. Haberer, R. Sharma, K. H. Lee, S. Nakamura, and E. L. Hu, Nat. Photonics **1**, 61 (2007).
6. Y. Yamamoto and R. E. Slusher, Phys. Today **46**(6), 66 (1993).
7. T. Someya, R. Werner, A. Forchel, M. Catalano, R. Cingolani, and Y. Arakawa, Science **285**, 1905 (1999).
8. R. A. Oliver, G. A. D. Briggs, M. J. Kappers, C. J. Humphreys, S. Yasin, J. H. Rice, J. D. Smith, and R. A. Taylor, Appl. Phys. Lett. **83**, 755 (2003).
9. H. A. R. El-Ella, F. Rol, D. P. Collins, M. J. Kappers, R. A. Taylor, E. L. Hu, and R. A. Oliver, J. Cryst. Growth **321**, 113 (2011).
10. T. Zhu, H. A. R. El-Ella, B. Reid, M. J. Holmes, R. A. Taylor, M. J. Kappers, and R. A. Oliver, J. Cryst. Growth **338**, 262 (2012).
11. N. Niu, A. Woolf, D. Wang, T. Zhu, Q. Quan, R. A. Oliver, and E. L. Hu, Appl. Phys. Lett. **106**, 231104 (2015).
12. R. A. Oliver, A. F. Jarjour, R. A. Taylor, A. Tahraoui, Y. Zhang, M. J. Kappers, and C. J. Humphreys, Mater. Sci. Eng. B **147**, 108 (2008).
13. A. F. Jarjour, R. A. Oliver, A. Tahraoui, M. J. Kappers, C. J. Humphreys, and R. A. Taylor, Phys. Rev. Lett. **99**, 197403 (2007).
14. G. Bjork and Y. Yamamoto, IEEE J. Quantum Electron. **27**, 2386 (1991).